



Accelerating Fe(III)/Fe(II) redox cycling in heterogeneous electro-Fenton process via S/Cu-mediated electron donor-shuttle regime

Chao Wang^a, Wenfeng Zhang^a, Jingwen Wang^a, Pan Xia^a, Xiaoguang Duan^{b,*}, Qiang He^a, Ignasi Sirés^c, Zhihong Ye^{a,*}

^a Key Laboratory of the Three Gorges Reservoir Region's Eco-Environment, Ministry of Education, College of Environment and Ecology, Chongqing University, Chongqing 400045, China

^b School of Chemical Engineering, The University of Adelaide, Adelaide, SA 5005, Australia

^c Laboratori d'Electroquímica dels Materials i del Medi Ambient, Departament de Ciència de Materials i Química Física, Secció de Química Física, Facultat de Química, Universitat de Barcelona, Martí i Franquès 1–11, 08028 Barcelona, Spain

ARTICLE INFO

Keywords:

Heterogeneous electro-Fenton
Fe(III)/Fe(II) cycling
Electron shuttle
Hydroxyl radicals
Nanocomposites

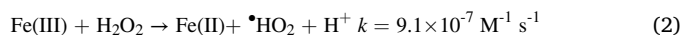
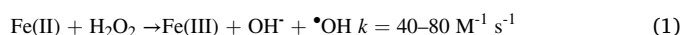
ABSTRACT

In this study, we developed a Cu_{0.5}Fe_{2.5}S₄ nanocatalyst through facile sulfidation of the Cu-MIL-88B(Fe) precursor to expedite surface Fe(III) reduction and enhance H₂O₂ activation in the heterogeneous electro-Fenton (HEF). The as-prepared catalyst possesses relatively large specific surface area and uniformly dispersed metal active sites. The Cu_{0.5}Fe_{2.5}S₄-catalyzed HEF system allowed complete removal of naproxen with minimal metal leaching, surpassing that of Cu-MIL-88B(Fe) or Fe₃S₄. Quantitative XPS analysis, electrochemical characterization and density functional theory calculations reveal an electron donor-shuttle regime in which S²⁻ and Cu species serve as the electron donor and shuttle, respectively. The Cu species significantly accelerate the internal electron transfer between S and Fe and mitigate the dissolution of the adjacent iron sites, securing the sustainable reducing capacity. Moreover, Cu_{0.5}Fe_{2.5}S₄-based HEF exhibits great practicability for treatment of various organics in urban wastewater. This study opens new avenue for addressing the challenge of sluggish Fe(III)/Fe(II) cycling in HEF.

1. Introduction

The electro-Fenton (EF) system has emerged as one of the most popular wastewater treatment technologies over the last decades, because EF allows producing H₂O₂ in-situ via a two-electron oxygen reduction reaction and subsequently yields highly oxidizing hydroxyl radicals ([•]OH, E⁰ = 2.8 V vs. SHE) via Fenton chemistry for degrading recalcitrant organic pollutants [1,2]. To scale-up this technology, the heterogeneous electro-Fenton (HEF) process, particularly based on iron solid catalysts, has been intensively studied due to advantages like wide reaction pH range, low sludge production and high recyclability of the catalyst [3,4]. In HEF, the electrogenerated H₂O₂ is activated by Fe(II)-containing catalysts in the solution to produce [•]OH heterogeneously (Eq. 1) [5]. Simultaneously, H₂O₂ acts as the electron donor, which reduces Fe(III) to Fe(II) to sustain the oxidation (Eq. 2) [6]. Nonetheless, the sluggish Fe(III)/Fe(II) redox cycle for continuous [•]OH production is the rate-limiting step determining the overall degradation efficiencies, because the kinetics of Eq. 1 is several orders of magnitude faster than

that of Eq. 2 [6,7]. Additionally, the product of Eq. 2, hydroperoxyl radical (HO₂[•], 1.7 V vs. SHE), is less powerful than [•]OH (2.8 V vs. SHE), and the rapid precipitation of inactive Fe(III) species in the form of iron oxy-hydroxides at the catalyst surface usually leads to the quick deactivation, greatly hampering their practical application [8].



Recently, several strategies have been explored to accelerate the reduction of Fe(III), including external energy stimuli (e.g. light and ultrasounds) [9,10] and the addition of chemical promoters (e.g. organic chelators and inorganic compounds) [11]. However, the additional cost induced by energy input limits its large-scale application. The iron organic chelators without intensive energy input appear more promising for the promotion of Fe(III) reduction [12]. For instance, polycarboxylates can modulate the redox potential of Fe(III)/Fe(II) couples, resulting in easier iron cycling [13]. However, these organic

* Corresponding authors.

E-mail addresses: xiaoguang.duan@adelaide.edu.au (X. Duan), yezhihong@cqu.edu.cn (Z. Ye).

<https://doi.org/10.1016/j.apcatb.2023.123457>

Received 5 September 2023; Received in revised form 27 October 2023; Accepted 30 October 2023

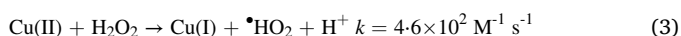
Available online 31 October 2023

0926-3373/© 2023 The Authors. Published by Elsevier B.V. This is an open access article under the CC BY license (<http://creativecommons.org/licenses/by/4.0/>).

compounds may compete with the target pollutants for $\cdot\text{OH}$, and their decomposition can cause secondary pollution. Alternatively, inorganic compounds like black phosphorus, zero-valent metal and boron powder with abundant reductive sites are appealing catalysts to accelerate the Fe(III)/Fe(II) redox cycle in homogeneous EF systems by donating sufficient electrons [14]. However, these additive methods often suffer from significant electron transfer losses and prove challenging to fully utilize, in contrast to bonded coupling through direct modification. The latter approach reduces the electron transfer distance and enhances overall catalyst stability.

In recent studies, direct sulfur modification has been demonstrated to be an effective strategy to accelerate the Fe(III)/Fe(II) redox cycling by leveraging the high electron-donating capacity of the low-valence S [15]. As reported, the surface sulfidation of $\beta\text{-FeOOH}$ (Fe_3S_4 @ $\beta\text{-FeOOH}$) can increase the degradation kinetics of heterogeneous Fenton system by 40 times [16]. Sulfidation of oolitic hematite led to the formation of FeS_2 , where the lattice S(II) on the surface greatly promoted the electron transfer between H_2O_2 and iron active sites, thereby enhancing the heterogeneous Fenton's reaction [17]. However, the continuous loss of effective sulfur sites and the high amount of leached iron ions due to the accompanying release of hydrogen ions still restrict its practical application. To achieve a sustainable sulfidation strategy, the employment of metal organic frameworks (MOFs) as precursors has emerged as a promising alternative due to their unique features such as large specific surface area (SSA), high porosity, and uniformly dispersed active sites [18,19]. Our previous work has demonstrated the excellent catalytic performance and stability of the sulfidized Fe-MOFs [20]. However, it was evident that the relatively low electron transfer efficiency between S and Fe continued to constrain the regeneration of Fe (II) during HEF.

Bimetallic MOFs can control the electronic structures of individual metal sites and thus regulate their catalytic activity [21,22]. The addition of redox-active metals such as Cu, Co, and Mn will not only accelerate the Fe(III)/Fe(II) redox cycle but themselves are Fenton-active elements to promote H_2O_2 decomposition to $\cdot\text{OH}$ [23,24]. Prior researches have explored the utilization of Cu-based MOFs in wastewater treatment due to the favorable compatibility between organic linkers and Cu nodes [25]. For instance, Wang et al. prepared an Fe-Cu bimetallic MOF material as an effective Fenton-like catalyst, which exhibited remarkable catalytic activity due to the synergistic effect between Fe and Cu species [26]. Moreover, the thermodynamically favorable reduction of Fe(III) by Cu(I) facilitates Fe(II) regeneration ($E_{\text{Cu(II)/Cu(I)}} = 0.17\text{ V}$ and $E_{\text{Fe(III)/Fe(II)}} = 0.77\text{ V}$ vs. NHE) [27], and the as-formed Cu(II) can be more readily reduced by H_2O_2 (Eq. 3) due to the higher kinetic constant compared to Eq. 2 [28]. Despite the fact that introducing Cu would accelerate the electron transfer during the reaction, this method still has the deficiencies of limited electron-donating capacity of Cu and the risk of secondary contamination arising from copper dissolution caused by the unsatisfactory water stability of the catalyst. Fortunately, considering the redox cycles of Cu(III)/Cu(II)/Cu(I), copper can also act as electron shuttle for Fe(III) reduction.



Inspired by this, the sulfidation of copper-doped MIL-88B(Fe) to obtain a new HEF catalyst ($\text{Cu}_{0.5}\text{Fe}_{2.5}\text{S}_4$) is proposed for the first time, where S and Cu act as the electron donor and shuttle, respectively. The two species are expected to significantly promote the Fe(III)/Fe(II) redox cycle, eventually achieving high-performance organic wastewater decontamination. The modulation of the electronic and chemical structure of the as-prepared catalyst was made by controlling the synthesis conditions. The catalytic performance of the optimized catalyst was thoroughly evaluated by treating naproxen and several micro-pollutants in the HEF system. The surface reactions and electron transfer among S, Cu and Fe were explored through electrochemical characterization, X-ray photoelectron spectroscopy (XPS) and DFT calculations to

disclose the relationship between the elemental redox states and the redox capacity, as well as reveal the origins of the enhanced activity. Hence, this work is expected to elucidate the key roles of sulfur and copper in accelerating the Fe(III)/Fe(II) redox cycle during HEF, providing a new strategy for the synthesis of highly active and stable catalysts for sustainable water decontamination.

2. Experimental section

2.1. Chemicals and materials

The details of the chemicals and materials used in this study are provided in the [Supplementary Data](#) (Text S1).

2.2. Catalyst synthesis

The synthesis route of $\text{Cu}_{0.5}\text{Fe}_{2.5}\text{S}_4$ is illustrated in [Fig. 1a](#). First, Cu-MIL-88B(Fe) with porous structure was prepared by the solvothermal method. Thereafter, the $\text{Cu}_{0.5}\text{Fe}_{2.5}\text{S}_4$ was obtained by the sulfidation of Cu-MIL-88B(Fe) precursor under controlled conditions. The specific procedures are as follows in subsections below.

2.2.1. Synthesis of Cu-MIL88B(Fe)

Cu-MIL-88B(Fe) was prepared following a typical solvothermal method. 10 mmol of $\text{FeCl}_3 \cdot 6\text{H}_2\text{O}$, a certain amount of $\text{Cu}(\text{NO}_3)_2$ and 10 mmol of H_2BDC were dissolved in 50 mL DMF to form a homogeneous solution. Then, 4 mL of NaOH aqueous solution (2 M) was added dropwise under vigorous stirring. The as-obtained mixed solution was then transferred into a Teflon-autoclave (75 mL) and heated at $100\text{ }^\circ\text{C}$ for 12 h. After cooling down, the fresh slurry was separated by centrifugation and washed with ultra-pure water and ethanol (3 times). The final Cu-MIL-88B(Fe) was collected by centrifugation and dried in a vacuum oven at $60\text{ }^\circ\text{C}$ for 12 h. Besides, different Cu/Fe mole ratio (1:1, 1:2, 1:5, 1:7, and 1:9) was employed to prepare the Cu-MIL-88B(Fe) precursor.

2.2.2. Synthesis of $\text{Cu}_{0.5}\text{Fe}_{2.5}\text{S}_4$

To prepare $\text{Cu}_{0.5}\text{Fe}_{2.5}\text{S}_4$, 300 mg Cu-MIL-88B(Fe) (prepared with the Cu/Fe ratio of 1:5) was suspended in 50 mL ethanol solution. After ultrasound treatment for 15 min, 1.20 g of thioacetamide (TAA) was added as the sulfur source to the solution under vigorous stirring for 15 min. The suspension was sealed in the Teflon-lined autoclave to conduct solvothermal treatment at $150\text{ }^\circ\text{C}$ for 4 h. After cooling down naturally, the black precipitates were collected by centrifugation and washed with ultra-pure water and ethanol 3 times each. The product was dried in a vacuum oven at $60\text{ }^\circ\text{C}$ for 12 h. Other catalysts prepared with Cu-MIL-88B(Fe) at different Cu/Fe ratios followed the same procedure.

2.3. Performance evaluation

The electrolytic experiments were carried out in a single chamber glass cell (160 mL) containing a 0.06 mM contaminants and 0.05 M Na_2SO_4 solution under magnetic stirring at the room temperature ([Fig. S1a](#)). The pollutant concentration is selected based on the previous study [29]. The cathode was a gas diffusion electrode made with carbon-polytetrafluoroethylene (PTFE) on carbon cloth to ensure efficient and continuous H_2O_2 production [30], whereas the anode was a commercial IrO_2 -based dimensionally stable anode ($\text{IrO}_2\text{-DSA}$) in most cases ([Fig. S1b](#)), although a boron-doped diamond thin film (Si|BDD) was employed to enhance the total organic carbon (TOC) abatement [31]. The geometric surface area of all the electrodes was 3 cm^2 and the interelectrode spacing was around 1.0 cm. The HEF experiment was initiated by adding a certain amount of catalyst to the solution and the supply of a constant current from a DC power supply (IT6302 from ITECH, China). During the reaction, 0.5 mL solution was sampled at regular intervals and then filtered with a Teflon syringe filter ($0.22\text{ }\mu\text{m}$)

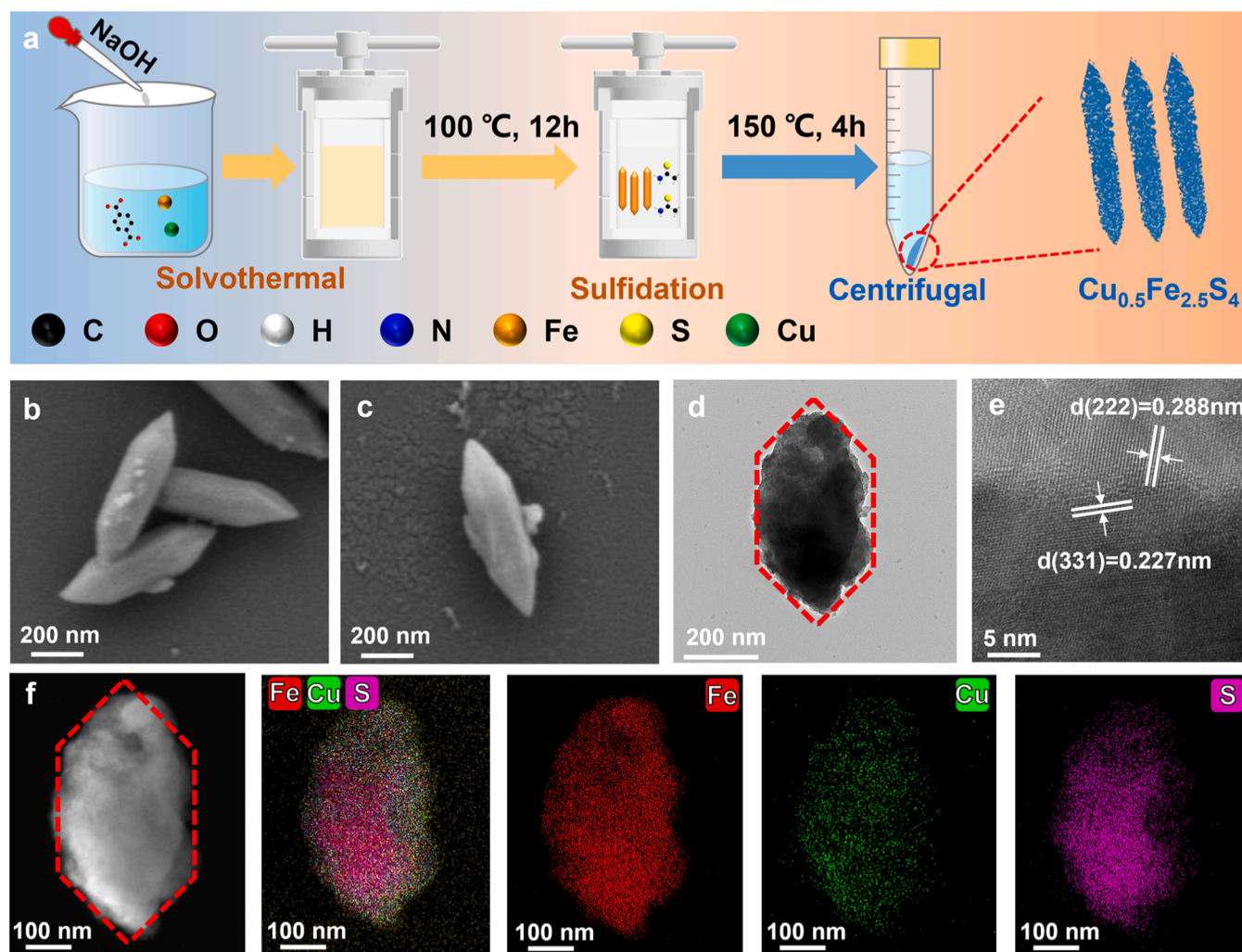


Fig. 1. (a) Schematic illustration of the synthetic route of $\text{Cu}_{0.5}\text{Fe}_{2.5}\text{S}_4$. SEM images of (b) MIL-88B(Fe) and (c) Cu-MIL-88B(Fe) (Cu/Fe=1/5). (d) TEM image of $\text{Cu}_{0.5}\text{Fe}_{2.5}\text{S}_4$. (e) The HRTEM image of $\text{Cu}_{0.5}\text{Fe}_{2.5}\text{S}_4$ and the corresponding (f) EDS mapping of Fe, Cu, S.

to remove impurities. For the cyclic tests, the used catalyst was magnetically separated by a permanent magnet, washed with ultrapure water and dried overnight in a vacuum oven at $60\text{ }^\circ\text{C}$.

2.4. Analytical methods

The surface morphological structure of the catalyst was observed by scanning electron microscopy (SEM, Zeiss Merlin Compact) and high-resolution transmission electron microscopy (HRTEM, Talos F200X). The microscope was coupled to an energy dispersive spectroscopy (EDS) detector for elemental mapping acquisition. The particle size distribution of the catalysts was analyzed by dynamic light scattering (DLS) (Malvern Zetasizer Nano ZS90). The X-ray diffraction (XRD) analysis was performed on an X-ray powder diffractometer (Rigaku SmartLab) at a rate of 2° min^{-1} with $\text{Cu-K}\alpha$ radiation (40 kV, 40 mA, range from 0° to 80°). The chemical states of different elements in the catalysts were analyzed by X-ray photoelectron spectroscopy (XPS) (Thermo Scientific K-Alpha spectrometer). The inductively coupled plasma optical emission spectrometry (ICP-AES, ICPS-8100, Shimadzu) analysis was used to determine the content of each element in the catalyst. Thermo Scientific Nicolet iS20 Fourier transform-infrared (FT-IR) spectrometer was employed to analyze the functional groups in the catalysts. The specific surface area was investigated using a Brunauer-Emmett-Teller (BET) analyzer. The magnetic property of the as-prepared catalyst was determined on a vibrating sample magnetometer (VSM) at 298 K. The

electron paramagnetic resonance (EPR) analysis of $\cdot\text{OH}$ was carried out with an EPR300E spectrometer (Bruker, Germany) using 5,5-dimethyl-1-pyrroline-N-oxide (DMPO) as the spin-trapping agent. Electrochemical impedance spectroscopy (EIS), linear polarization, cyclic voltammetry (CV) and open-circuit potential analysis were carried out on a CHI 760E electrochemical workstation. Detailed information on electrochemical measurements can be found in the [Supplementary Data](#) (Text S2).

The solution pH was measured with a PHS-3 C pH-meter. The concentrations of the treated pollutants were determined by a high-performance liquid chromatography (HPLC, SCION6000, China) with a C18 column ($4.6 \times 250\text{ mm}$, $5\text{ }\mu\text{m}$). The details can be found in [Supplementary Data](#) (Text S3). The H_2O_2 concentration was measured from the absorbance of the complex formed between the oxidant and Ti(IV) using a UNIC UV2365 spectrophotometer ($\lambda = 408\text{ nm}$) [30]. The dissolved iron concentration was determined from the absorbance of the reddish complex formed once reacted with 1,10-phenanthroline using the same spectrophotometer ($\lambda = 510\text{ nm}$). The TOC content was analyzed by a Shimadzu TOC-L analyzer. The degradation intermediates of naproxen (NPX) were identified by liquid chromatography-hybrid quadrupole time-of-flight mass spectrometry (LC-QTOF-MS) analysis. The DFT calculations were carried out with the Vienna Ab-initio simulation package (VASP), and the details are provided in [Supplementary Data](#) (Text S4).

3. Result and discussion

3.1. Synthesis and characterization of catalyst

The SEM analysis of MIL-88B(Fe) in Fig. 1b reveals its typical spindle shape with a length of around 500 nm. Moreover, the partial substitution of Fe sites by Cu did not alter the morphology and particle size of MIL-88B(Fe) (Fig. 1c) [32]. The TEM analysis in Fig. 1d shows that the $\text{Cu}_{0.5}\text{Fe}_{2.5}\text{S}_4$ basically inherited the morphology and dimensions of Cu-MIL-88B(Fe), but the surface became rough, which indicates the robustness of the $\text{Cu}_{0.5}\text{Fe}_{2.5}\text{S}_4$ framework thanks to the strong coordination structure of the MOF precursor [20]. In addition, the DLS analysis of $\text{Cu}_{0.5}\text{Fe}_{2.5}\text{S}_4$ displays an average size of around 470 nm (Fig. S2), which is in good agreement with the particle size observed in TEM image. Further HRTEM images in Fig. 1e show the well-defined lattice fringes with *d*-spacings of 0.23 nm and 0.29 nm, corresponding to the lattice spacing of (222) and (331) crystal planes of $\text{Cu}_{0.5}\text{Fe}_{2.5}\text{S}_4$, respectively, which confirms the high crystallinity of $\text{Cu}_{0.5}\text{Fe}_{2.5}\text{S}_4$ [33]. The EDS mapping results in Fig. 1f demonstrate the uniform distribution of Fe, Cu and S elements throughout the catalyst.

The XRD patterns of the as-prepared catalysts were investigated to clarify their crystalline structures. As shown in Fig. 2a, the main peaks of MIL-88B(Fe) are in excellent agreement with the simulated diffractogram, indicating its successful fabrication [34]. Cu-MIL-88B(Fe) displays almost identical patterns to MIL-88B(Fe), confirming that Cu-MIL-88B(Fe) maintains the original crystalline structure after Cu doping. The catalyst obtained from the sulfidation of MIL-88B(Fe) is characterized by peaks at 25.4° , 30.0° , 31.3° , 36.3° , 39.8° , 44.9° , 47.8° and 52.4° , which can be attributed to (220), (311), (222), (400), (331) (422), (511) and (440) crystal planes of Fe_3S_4 , indicating that the hydrothermal sulfidation treatment of MIL-88B(Fe) with TAA results in Fe_3S_4 as the final product [35]. Notably, the positions of all the diffraction peaks of the as-prepared $\text{Cu}_{0.5}\text{Fe}_{2.5}\text{S}_4$ also matched well with

the standard card of Fe_3S_4 (JCPDS card No.16-0713) with no peaks indexed to copper oxides. Nonetheless, the peak intensities of (222) and (331) crystal planes increase significantly, which is consistent with the TEM images, suggesting that Cu doping induced the changes in crystal growth orientations.

Moreover, no obvious variation was found in the FTIR spectra of MIL-88B(Fe) and Cu-MIL-88B(Fe) (Fig. S3), suggesting that the incorporation of Cu barely affected the functional groups of MIL-88B(Fe). The peaks located at 1657, 1600 and 1393 cm^{-1} are attributed to the C=O tensile shock, asymmetric vibration and symmetric vibration of carboxylate groups. The peaks at 3430 cm^{-1} and 749 cm^{-1} are attributed to the O-H stretching and C-H bending vibrations, respectively [36]. The adsorption peak at 551 cm^{-1} is assigned to the Fe-O (Cu-O) stretching mode originating from the link between metal and the ligand.

The chemical states of Fe_3S_4 and $\text{Cu}_{0.5}\text{Fe}_{2.5}\text{S}_4$ were surveyed by XPS analysis. As shown in Fig. 2b, the high resolution Fe 2*p* spectra of Fe_3S_4 and $\text{Cu}_{0.5}\text{Fe}_{2.5}\text{S}_4$ exhibited two splitting peaks at binding energies of 714.2 and 728.6 eV corresponded to Fe 2*p*_{3/2} and Fe 2*p*_{1/2} of Fe(III), indicating the presence of Fe(III)-S species, whereas the peaks appearing at 711.1 and 724.4 eV can be ascribed to Fe(II)-S species [37]. The results confirmed the conversion of Fe(III) to Fe(II) by acquiring electrons from S^{2-} during the sulfidation process (Table S1). Notably, the proportion of Fe(II) species in $\text{Cu}_{0.5}\text{Fe}_{2.5}\text{S}_4$ was slightly lower than that in Fe_3S_4 (68% vs. 76%), which was due to the fact that the doped Cu(II) species competed for electrons with Fe(III), capitalizing on its higher electronegativity (Fe (1.8) < Cu (1.9)) [38]. The S 2*p* spectra of Fe_3S_4 and $\text{Cu}_{0.5}\text{Fe}_{2.5}\text{S}_4$ in Fig. 2c illustrate five splitting peaks at 160.8, 162.1, 163.4, 164.9 and 168.5 eV, which can be assigned to $\text{S}_{\text{bulk}}^{2-}$, $\text{S}_{\text{surface}}^{2-}$, S_{n}^{2-} , S^0 and SO_4^{2-} , respectively. The reduction of Fe(III)/Cu(II) during the sulfidation process was accompanied by the oxidation of S^{2-} species, giving rise to the production of S_{n}^{2-} [39]. The formation of S^0 and SO_4^{2-} was also attributed to the redox reactions between $\text{S}^{2-}/\text{S}_{\text{n}}^{2-}$ and Fe(III)/Cu(II) (details can be seen in Section 3.3) [40]. Additionally, Fig. 2c witnessed

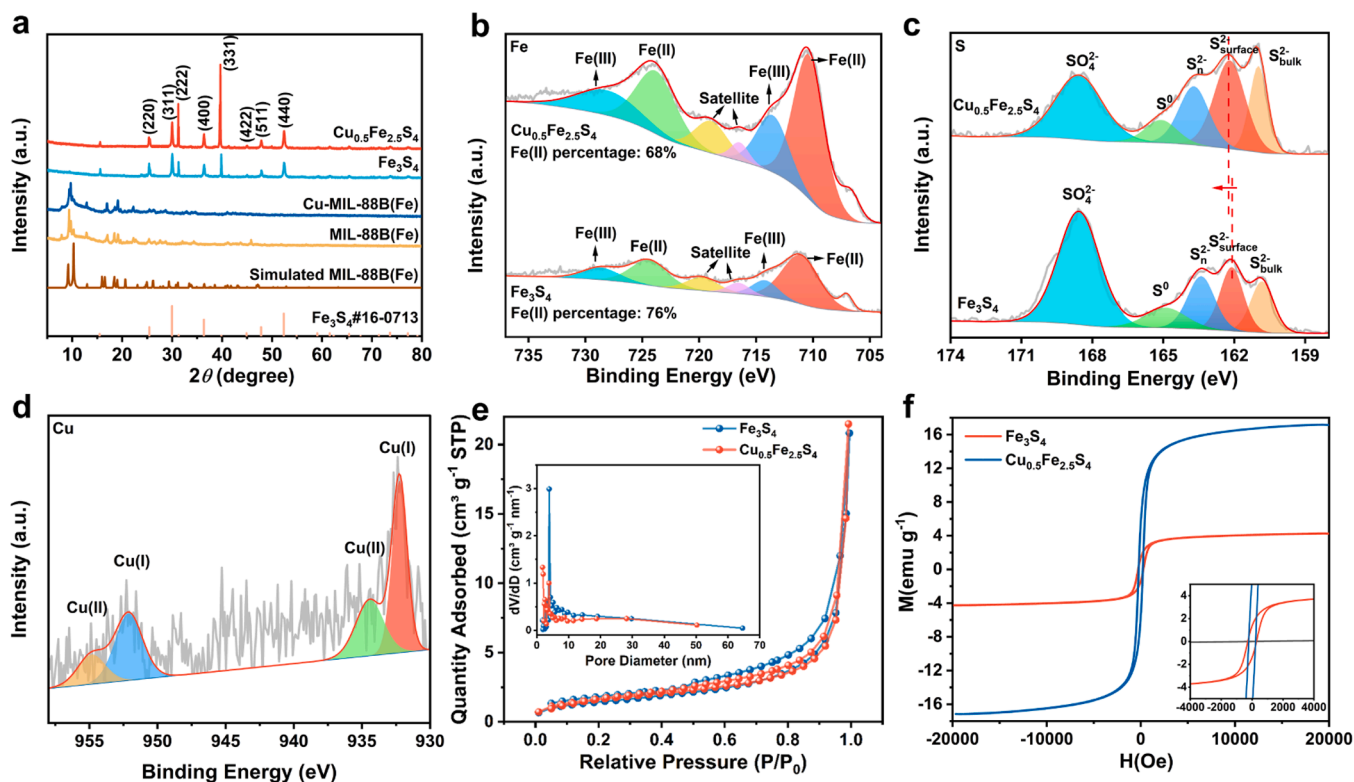


Fig. 2. (a) XRD patterns of MIL-88B(Fe), Fe_3S_4 and $\text{Cu}_{0.5}\text{Fe}_{2.5}\text{S}_4$. XPS spectra of $\text{Cu}_{0.5}\text{Fe}_{2.5}\text{S}_4$ and Fe_3S_4 in the regions of (b) Fe 2*p* and (c) S 2*p*, and the (d) Cu 2*p* XPS spectrum of $\text{Cu}_{0.5}\text{Fe}_{2.5}\text{S}_4$. (e) N_2 adsorption-desorption isotherms, pore size distribution curves (the inset in plot (e)), and (f) magnetization hysteresis curves of $\text{Cu}_{0.5}\text{Fe}_{2.5}\text{S}_4$ and Fe_3S_4 .

that S 2p peaks slight shifted towards higher binding energies in $\text{Cu}_{0.5}\text{Fe}_{2.5}\text{S}_4$, signifying the enhanced electron transfer from S to the bonded metals. In the Cu 2p spectrum of $\text{Cu}_{0.5}\text{Fe}_{2.5}\text{S}_4$ (Fig. 2d), the peaks centered at 932.7 and 952.4 eV can be ascribed to Cu(I), whereas the peaks at 934.7 and 955.3 eV correspond to Cu(II). Notably, the Cu-MIL-88B(Fe) precursor contains copper centers in the Cu(II) state [41]. The percentage of Cu(I) in $\text{Cu}_{0.5}\text{Fe}_{2.5}\text{S}_4$ was much higher than that of Cu(II) species (65% vs. 35%), confirming that Cu(II) can efficiently acquire electrons from S during the sulfidation treatment [42]. Moreover, the Cu/Fe mole ratio in $\text{Cu}_{0.5}\text{Fe}_{2.5}\text{S}_4$ was confirmed to be 1:5 by ICP-AES analysis (Table S2).

The nitrogen absorption-desorption isotherms of $\text{Cu}_{0.5}\text{Fe}_{2.5}\text{S}_4$ and Fe_3S_4 were also analyzed. The two samples exhibited type IV isotherms, accounting for the presence of abundant mesoporous structure (Fig. 2e). $\text{Cu}_{0.5}\text{Fe}_{2.5}\text{S}_4$ has a higher SSA ($5.9 \text{ m}^2 \text{ g}^{-1}$) and a small average pore size (7.6 nm), compared with Fe_3S_4 ($5.2 \text{ m}^2 \text{ g}^{-1}$, 9.2 nm). These variations may be attributed to the increase in pore space after doping with Cu. The relatively high specific surface area and porous nature favor the mass transport of H_2O_2 and pollutants and the exposure of more active sites, which facilitates the activation of H_2O_2 for $\cdot\text{OH}$ production and the subsequent pollutants degradation. Furthermore, the magnetic saturation value of $\text{Cu}_{0.5}\text{Fe}_{2.5}\text{S}_4$ (Fig. 2f) recorded by the vibrating sample magnetometer was 17.2 emu g^{-1} , which is considerably higher than that of Fe_3S_4 (4.2 emu g^{-1}). The remarkable magnetism of $\text{Cu}_{0.5}\text{Fe}_{2.5}\text{S}_4$ enables its easy separation from the HEF system using only an external magnetic field, confirming its technical and economic feasibility in practical application. [43].

3.2. Evaluation of catalytic performance

The degradation of naproxen (NPX) by different systems was comparatively investigated to evaluate the catalytic activity and

stability of $\text{Cu}_{0.5}\text{Fe}_{2.5}\text{S}_4$. The presence of $0.10 \text{ g L}^{-1} \text{ Fe}_3\text{S}_4$ and $\text{Cu}_{0.5}\text{Fe}_{2.5}\text{S}_4$ only yielded negligible NPX removal of 6.6% and 11.6%, respectively, implying that the adsorption of NPX can be neglected during the subsequent electrochemical trials (Fig. S4). As depicted in Fig. 3a, the electro-oxidation process resulted in a paltry 20.0% abatement of NPX in 60 min because of the low oxidation power of $\text{IrO}_2(\cdot\text{OH})$ produced at the surface IrO_2 -DSA plate. The MIL-88B(Fe) attained an enhanced degradation of 30.8% at 90 min, and the unsatisfactory catalytic performance was due to the lack of sufficient unsaturated iron active sites that are well coordinated by the organic ligands and slow Fe (III)/Fe(II) redox cycling. The degradation efficiency increased to 41.7% with Cu-MIL 88B(Fe), revealing the crucial role of the internal electron transfer between Cu and Fe in promoting Fe(III) reduction. Surprisingly, the Fe_3S_4 catalyzed HEF only achieved a slight enhancement in NPX removal (36.7%) compared to MIL-88B(Fe), although the Fe(III)/Fe(II) redox cycling was expected to be accelerated due to the presence of abundant S^{2-} electron donors. In fact, the complete sulfidation also led to severe collapse of the MIL-88B(Fe) skeleton (Fig. S5), and the sulfidation treatment can destabilize the iron sites by decreasing the corrosion potential of Fe, which accelerated the dissolution of iron ions [44]. The precipitation of the dissolved iron at the catalyst surface may poison the active sites, thus reducing NPX degradation kinetics. In contrast, the $\text{Cu}_{0.5}\text{Fe}_{2.5}\text{S}_4$ -catalyzed HEF system displayed the best performance, achieving 100% NPX decay in 60 min. The corresponding kinetic calculations for the electrochemical trials fitted well with a pseudo-first order kinetics, and the highest rate constant of 0.034 min^{-1} was obtained in the $\text{Cu}_{0.5}\text{Fe}_{2.5}\text{S}_4$ -catalyzed HEF process, being around 4.4-fold greater than that of HEF with Fe_3S_4 (Fig. S6). Moreover, as mentioned above, Fe_3S_4 still suffered from low stability with a high iron leaching of 3.6 mg L^{-1} . A relatively low iron leaching of 1.7 mg L^{-1} from $\text{Cu}_{0.5}\text{Fe}_{2.5}\text{S}_4$ can be observed in Fig. 3b, demonstrating that the Cu doping not only significantly boosted the HEF performance, but also improved the

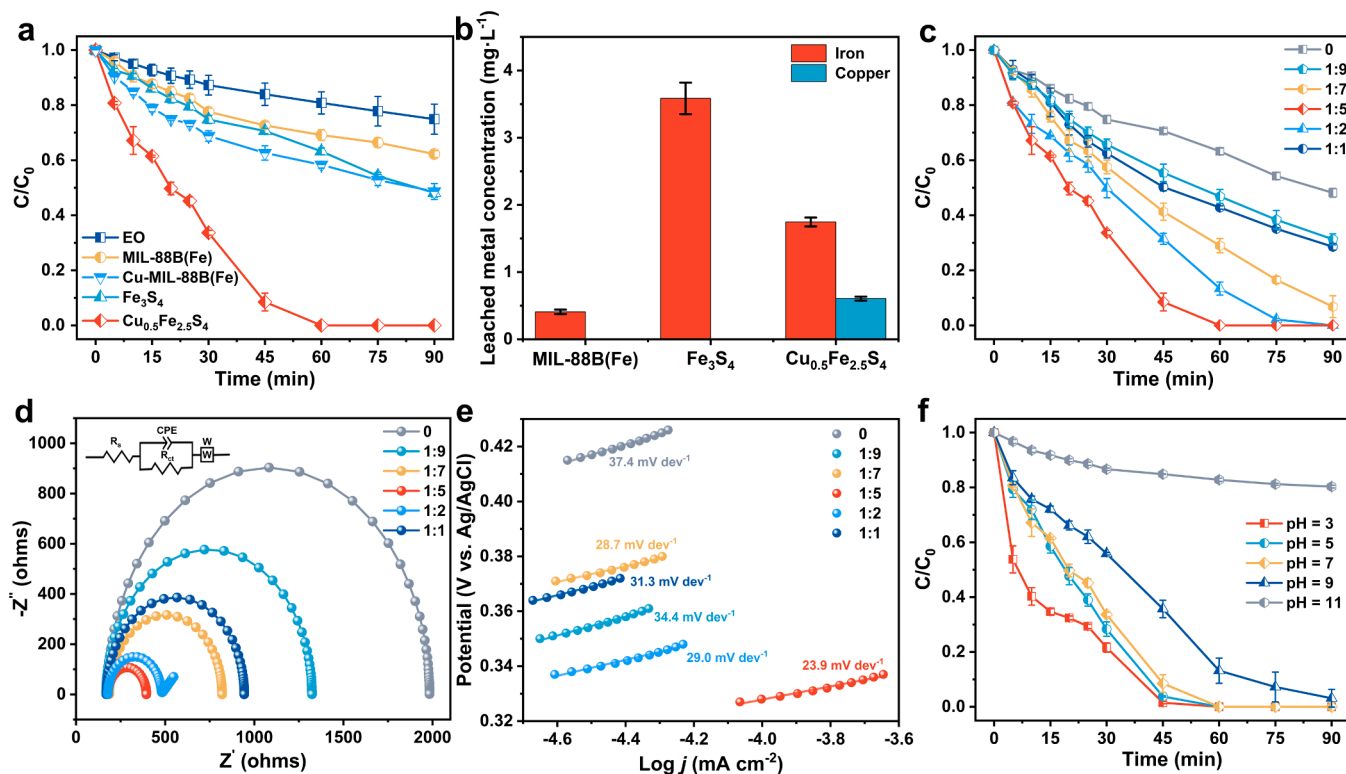


Fig. 3. (a) Normalized NPX decay during the treatments of 160 mL drug solutions with 0.05 M Na_2SO_4 by different reaction systems. (b) Leached iron and copper concentrations after 90 min of the trials in plot. (c) Effects of Cu/Fe ratio during the catalyst synthesis on the catalytic performance of HEF. (d) EIS and (e) Tafel plots of different catalysts in plot (c). (f) Effects of initial pH on NPX decay in the $\text{Cu}_{0.5}\text{Fe}_{2.5}\text{S}_4$ catalyzed HEF system. General conditions: $[\text{NPX}]_0 = 0.060 \text{ mM}$; $[\text{Catalyst}] = 0.10 \text{ g L}^{-1}$; Current = 50 mA; Initial pH = 7.0.

structural stability of the catalyst. This can be attributed to the fact that the Cu doping may increase the corrosion potential of Fe, thereby improving its stability [45].

The Cu/Fe ratio during the catalyst synthesis is one of the critical factors that affect the catalytic performance. As shown in Fig. 3c, the increase in Cu content yielding Cu/Fe ratios from 1:9 to 1:5 resulted in a substantial enhancement in the degradation of NPX, promoting the removal efficiency from 68.8% to 100% and rate constant from 0.013 min^{-1} to 0.034 min^{-1} (Fig. S7a). Nonetheless, the NPX decay dropped to 71.5%, when further increasing the ratio to 1:1. An optimal amount of Cu can accelerate the Fe(III)/Fe(II) redox cycling by acting as the electron shuttle during the HEF process, thereby enhancing the overall degradation efficiency of NPX. However, ultrahigh Cu loading is detrimental to the catalytic activity because of the significantly reduced population of surface iron active sites and the alteration of crystal structure bonding strength and electronic features of the catalyst. These observations are in good agreement with the XRD results in Fig. S7b. The highest diffraction peak intensities were achieved at the ratio of 1:5, suggesting the highly exposed active surface and crystal planes [33]. In addition, the Fe leaching during the reaction significantly decreased with the increase in Cu content, implying the enhanced stability of the catalyst by Cu doping (Fig. S7c). Meanwhile, the Cu leaching was kept very low in all cases ($< 1.0 \text{ mg L}^{-1}$). Note that the Fe and Cu leaching was 1.7 and 0.60 mg L^{-1} at the ratio of 1:5, respectively, lower than the European Union standard of 2 mg L^{-1} [20]. Moreover, the EIS and Tafel tests were carried out to evaluate the electron transfer capability of these catalysts. As shown in Fig. 3d and Table S3, the interfacial charge transfer resistance (R_{ct}) is acquired from the fitting of the corresponding equivalent circuit, and the lowest R_{ct} value was obtained at the ratio of 1:5 (214Ω). The outcomes demonstrate that an appropriate amount of Cu doping greatly promotes the internal electron transfer [46]. Similarly, the Tafel slope of the catalyst prepared at the Cu/Fe ratio of 1:5 was also the lowest (23.9 mV dec^{-1} , Fig. 3e), which corroborated the fastest electron transfer [7]. These favorable features support the superior catalytic performance in the experiments (Fig. 3c). The high electron transfer efficiency of the catalyst contributes to the Fe(III)-to-Fe(II) conversion, leading to better redox performance in HEF.

The impacts of various reaction parameters on NPX degradation during the $\text{Cu}_{0.5}\text{Fe}_{2.5}\text{S}_4$ -catalyzed HEF process were further investigated. As expected, the NPX decay increased from 47.6% to 100% when increasing the catalyst dosage from 0.05 to 0.1 g L^{-1} , with a slight rise in iron leaching from 1.1 to 1.7 mg L^{-1} (Figs. S8a and S8b). This was due to the increased number of active sites for H_2O_2 activation to produce more $\bullet\text{OH}$. A further increase in the dosage to 0.15 g L^{-1} failed to further enhance the NPX degradation and led to a higher iron leaching of 2.5 mg L^{-1} (Fig. S8b). This is because the excessive metal sites would compete for $\bullet\text{OH}$, thereby hampering the $\bullet\text{OH}$ attack on NPX [47]. As shown in Fig. S8c, when the applied current increased from 10 mA to 50 mA , the NPX removal was enhanced from 71.1% to 100% in 60 min, and the k_{obs} values risen from 0.017 to 0.040 min^{-1} (Fig. S8d). The better degradation performance is associated to the greater H_2O_2 production at higher current (Fig. S8e), with the consequent acceleration of Fenton's reaction. Nevertheless, the enhancement in NPX degradation was insignificant at the current of 75 mA due to the parasitic reaction between excessive H_2O_2 and $\bullet\text{OH}$ to produce $\bullet\text{O}_2$ (-0.33 V vs. SHE), giving rise to a reduction in the oxidative capacity of the system [8]. Fig. 3f and Fig. S8f show that complete NPX removal in 60 min can be observed at a wide initial pH range of 3.0–7.0, although the highest k_{obs} value of 0.040 min^{-1} was obtained at initial pH 3.0. The total NPX removal at initial pH 9.0 can still be achieved by extending the treatment time to 90 min. However, further increasing the initial pH to 11.0 led to a drastic deceleration of NPX decay, only attaining 18.3% due to the self-decomposition of H_2O_2 and lower oxidation potential of $\bullet\text{OH}$ at alkaline pH [48]. On the other hand, very low iron leaching of 1.9 and 1.7 mg L^{-1} was observed at initial pH 5.0 and 7.0, respectively, corroborating both the high activity and stability of $\text{Cu}_{0.5}\text{Fe}_{2.5}\text{S}_4$ at

near-neutral pH (Fig. S8f). Note that the solution pH will decrease over the course of reaction for all the cases due to the formation of acidic intermediates like carboxylates, which are non-toxic and can be easily biodegraded (Figs. S7c, S8b and S8f) [49]. Moreover, the removal of NPX with initial concentrations ranging from 0.030 to 0.24 mM was investigated (Fig. S9). Notably, the NPX removal exceeded 90% within the concentrations of 0.030 , 0.060 and 0.12 mM , primarily attributed to the presence of abundant $\bullet\text{OH}$. However, the removal efficiency decreased to 71.5% at the initial concentration of 0.24 mM , demonstrating that the available $\bullet\text{OH}$ was insufficient for degrading high concentration pollutants. Therefore, extended treatment time, higher current or a larger amount of catalyst is required to achieve satisfactory performance.

To identify the degradation pathway of NPX during the $\text{Cu}_{0.5}\text{Fe}_{2.5}\text{S}_4$ -catalyzed HEF process, the main intermediates were analyzed by LC-QTOF-MS (summarized in Table S4). Fig. S10 depicts the degradation routes proposed from the 14 detected by-products. First, the demethylation of the methoxy group in the side chain of NPX yielded compound P1, with a further decarboxylation to produce P2. The direct hydroxylation at the benzene ring and the alkyl carbon in the side chain of NPX led to products P3 and P4, respectively. The oxidation of P4 by $\bullet\text{OH}$ gave rise to P5, which could arise directly from the decarboxylation of NPX as well. Further oxidation of P5 led to the generation of P6 and P7, while the demethylation of P5 could also produce P2. On the other hand, the detachment of methoxy group from NPX by $\bullet\text{OH}$ attack generated compound P8, whose naphthalene ring is cleaved to yield the benzene derivatives P10 and P11. The $\bullet\text{OH}$ attack at the benzyl position of NPX formed compound P9, followed by hydroxylation, oxidation and detachment reactions to produce P12–14 [50].

3.3. Acceleration of Fe(III)/Fe(II) redox cycling

The electron transfer capability of the catalysts was explored using several electrochemical techniques. The open-circuit potential analysis in Fig. S11 highlights a higher potential of Fe(III) in $\text{Cu}_{0.5}\text{Fe}_{2.5}\text{S}_4$ than that in Fe_3S_4 (0.169 V vs 0.154 V), affirming the higher activity to produce Fe(II) that results in the stronger oxidation capacity of the $\text{Cu}_{0.5}\text{Fe}_{2.5}\text{S}_4$ -catalyzed HEF system [51]. Moreover, the CV curves further confirmed the facilitated Fe(III)/Fe(II) cycling due to the incorporation of Cu. As shown in Fig. 4a, obvious oxidation and reduction peaks appeared at 0.06 and 0.24 V with $\text{Cu}_{0.5}\text{Fe}_{2.5}\text{S}_4$, implying the excellent reversibility of the Fe(III)/Fe(II) redox process. In addition, the Cu-doping led to a decrease in peak-to-peak separation (ΔE_p) from 0.54 V to 0.18 V , indicating the improved Fe(III)/Fe(II) redox capability of $\text{Cu}_{0.5}\text{Fe}_{2.5}\text{S}_4$ [6]. As a result, the elevated potential of Fe(III) and facilitated Fe(III)/Fe(II) cycles in $\text{Cu}_{0.5}\text{Fe}_{2.5}\text{S}_4$ boosted the Fe(II) regeneration to further enhance the $\bullet\text{OH}$ production. Furthermore, the in-situ electrode potential analysis was also conducted to investigate the electron transfer during H_2O_2 activation. As shown in Fig. 4b, the addition of H_2O_2 triggered the increase in open-circuit potentials for both $\text{Cu}_{0.5}\text{Fe}_{2.5}\text{S}_4$ and Fe_3S_4 due to the immediate electron transfer from active sites to the adsorbed H_2O_2 . Notably, this increase was more significant with $\text{Cu}_{0.5}\text{Fe}_{2.5}\text{S}_4$, indicating a more rapid mass and electron transfer during H_2O_2 activation [52]. Upon the addition of NPX, the potentials with both $\text{Cu}_{0.5}\text{Fe}_{2.5}\text{S}_4$ and Fe_3S_4 decreased, because the surface-bound $\bullet\text{OH}$ ($\bullet\text{OH}_{\text{ads}}$) generated by H_2O_2 activation acquired electrons from NPX. The more significant decrease in the potential with $\text{Cu}_{0.5}\text{Fe}_{2.5}\text{S}_4$ demonstrates the faster electron transfer between NPX and the catalyst. These results reveal that the synergistic effect of Cu-doping on boosting HEF performance can be primarily attributed to the promoted electron transfer. Moreover, The EPR spectrum depicted in Fig. S12 shows the four typical peaks of DMPO- $\bullet\text{OH}$ adduct with an intensity ratio of 1:2:2:1, demonstrating the dominant role of $\bullet\text{OH}$ in $\text{Cu}_{0.5}\text{Fe}_{2.5}\text{S}_4$ -catalyzed HEF system. Additionally, the major contribution of $\bullet\text{OH}_{\text{ads}}$ to the degradation of NPX was confirmed by means of radical scavenging experiments, where *n*-butanol was used to scavenge all the

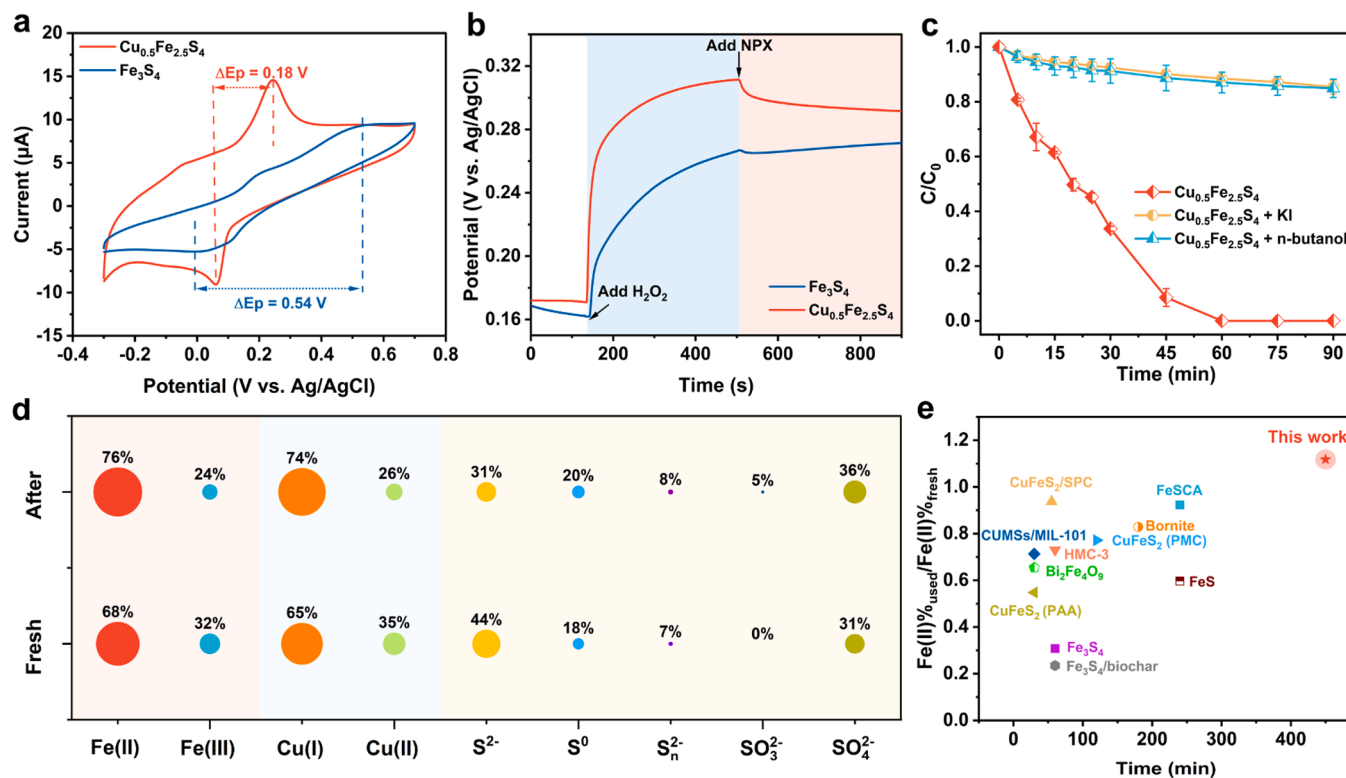


Fig. 4. (a) Cyclic voltammograms on Fe_3S_4 and $\text{Cu}_{0.5}\text{Fe}_{2.5}\text{S}_4$ coated glassy carbon electrode. (b) Open-circuit potential curves with the addition of H_2O_2 and NPX for Fe_3S_4 and $\text{Cu}_{0.5}\text{Fe}_{2.5}\text{S}_4$. (c) Effect of radical scavengers on NPX degradation (10 mM KI, 300 mM *n*-butanol). (d) The element concentrations of fresh and used $\text{Cu}_{0.5}\text{Fe}_{2.5}\text{S}_4$ catalyst. (e) The ratio of Fe(II) percentages in the used/fresh catalysts during different catalytic processes.

$\cdot\text{OH}$ (both $\cdot\text{OH}_{\text{ads}}$ and $\cdot\text{OH}_{\text{free}}$) and KI was employed to scavenge only $\cdot\text{OH}_{\text{ads}}$ [53]. As illustrated in Fig. 4c, the presence of excess *n*-butanol and KI led to a significant decrease in NPX abatement, reaching 15.1% and 14.6%, respectively, with negligible difference between them. This observation demonstrates that the major contribution to NPX degradation corresponds to $\cdot\text{OH}_{\text{ads}}$ rather than $\cdot\text{OH}_{\text{free}}$ in $\text{Cu}_{0.5}\text{Fe}_{2.5}\text{S}_4$ -catalyzed HEF system.

The XPS analysis of fresh and used $\text{Cu}_{0.5}\text{Fe}_{2.5}\text{S}_4$ (after five cycles) was conducted to clarify the role of S and Cu species in contributing to the Fe(III)/Fe(II) redox cycling. As depicted in Fig. S13a, the peak positions of the major elements were not substantially altered upon usage, implying the stable structure of the catalyst along the treatment. Nonetheless, the proportion of various forms of Fe, Cu and S species changed during the reaction (Fig. 4d). After cycling usage, the percentage of Cu(I) increased from 65% to 74%, as deduced from Fig. S13b, suggesting the continuous reduction of Cu(II) to Cu(I) by accepting electrons from S^{2-} ($E_{\text{Cu(II)/Cu(I)}} = 0.17$ V vs. NHE). Meanwhile, the percentage of Fe(II) increased from 68% to 76% despite its intense consumption by Fenton's reaction (Fig. 4d and Fig. S13c), which demonstrates that the regeneration rate of Fe(II) was much higher than its consumption rate during Fenton's reaction. Regarding the S species, Fig. 4d and Fig. S13d highlight a significant decrease in the content of S^{2-} (13%) and an increase in the amounts of oxidized sulfur species (S_n^{2-} , S^0 and SO_4^{2-}), confirming that S^{2-} could act as an electron donor to promote the reduction of Cu(II) and Fe(III) [54]. Notably, the ratio of Fe(II) percentages (i.e. used/fresh $\text{Cu}_{0.5}\text{Fe}_{2.5}\text{S}_4$ catalyst) reached a value as high as 1.1, meaning that the reduction of Fe(III) occurred at a faster rate than the Fe(II) consumption during the catalytic reaction. The result surpasses that of many previously reported catalysts in terms of boosting Fe(III)/Fe(II) redox cycling (Fig. 4e and Table S5), primarily because the electron shuttle role of Cu significantly enhances the electron transfer efficiency between S^{2-} and Fe(III). In contrast, the Fe 2p and S 2p XPS spectra of the fresh and used Fe_3S_4 are depicted in Fig. S14. Although a substantial decrease in the S^{2-}

content (18%) can be observed (Fig. S14a), the percentage of Fe(II) decreased by 7% during the reaction (Fig. S14b). The results further demonstrate the key role of Cu species, acting as the electron shuttle to accelerate the electron transfer between S^{2-} and Fe(III).

DFT calculations were performed to gain insights into the charge transfer in the catalysts, aiming at comprehensively proving the intricate catalytic mechanism. The optimized crystal structures of Fe_3S_4 and $\text{Cu}_{0.5}\text{Fe}_{2.5}\text{S}_4$ are shown in Fig. S15. The bond length of Fe-S in $\text{Cu}_{0.5}\text{Fe}_{2.5}\text{S}_4$ is shorter than that in Fe_3S_4 (2.21 Å vs 2.28 Å), which favors the electron transfer during the reaction and improves the stability of $\text{Cu}_{0.5}\text{Fe}_{2.5}\text{S}_4$ [55]. The total density of states (TDOS) analysis suggests zero-bandgap metallicity of both Fe_3S_4 and $\text{Cu}_{0.5}\text{Fe}_{2.5}\text{S}_4$, implying their favorable electrical conductivity and easy electron transfer (Fig. 5a). In addition, the position of the d-band center significantly affects H_2O_2 adsorption on the catalyst surface, as it determines the degree of electron filling in the antibonding state. Specifically, the d-band center of $\text{Cu}_{0.5}\text{Fe}_{2.5}\text{S}_4$ (−1.71 eV) is closer to the Fermi energy level than that of Fe_3S_4 (−2.68 eV), implying the higher energy of its d-orbital electrons. This leads to an increase in the adsorption energy between H_2O_2 and the catalyst surface, thus improving the overall catalytic performance of HEF [56]. Additionally, Cu doping induces an elevation in the p-band center of S, resulting in a considerable reduction in the difference between the $\epsilon_{\text{Fe-3d}}$ and $\epsilon_{\text{S-2p}}$ ($\epsilon_{\text{Fe-3d}}$ and $\epsilon_{\text{S-2p}}$ represent the Fe 3d and S 2p centers, respectively). The smaller p-d band difference endows $\text{Cu}_{0.5}\text{Fe}_{2.5}\text{S}_4$ with the high electron transfer efficiency for H_2O_2 activation (Fig. 5b and S16) [57].

Furthermore, Bader charge analysis shows significant charge accumulation at the S sites in $\text{Cu}_{0.5}\text{Fe}_{2.5}\text{S}_4$ and Fe_3S_4 due to the higher electronegativity of S. During the HEF process, there is a notable reduction in the charge density around S atoms, coupled with the increase in the charge densities of Cu and Fe atoms within $\text{Cu}_{0.5}\text{Fe}_{2.5}\text{S}_4$, confirming the occurrence of the electron transfer from S to Cu and Fe atoms (Fig. 5c). Interestingly, the decrease in charge around the S atoms

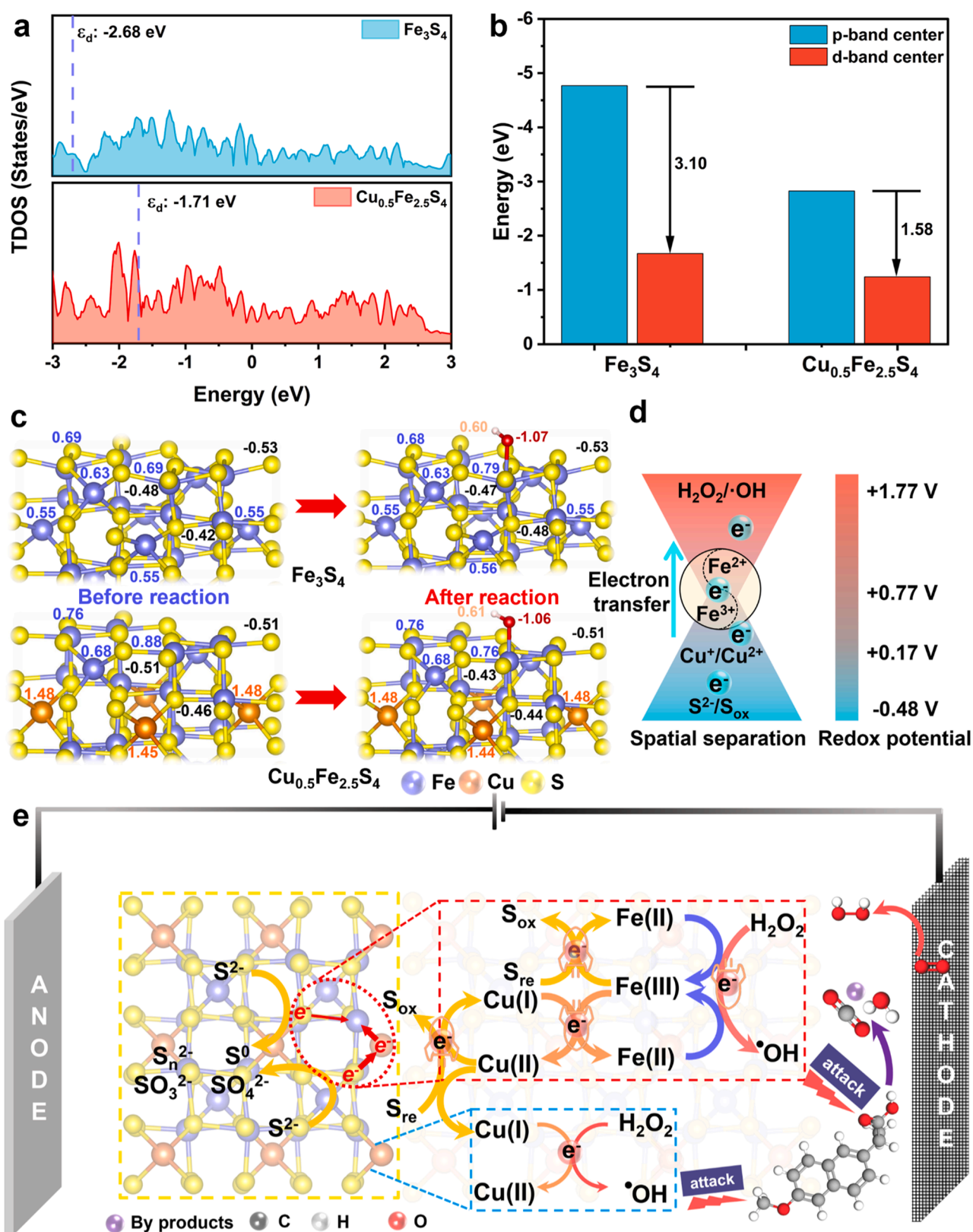
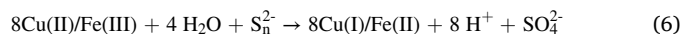
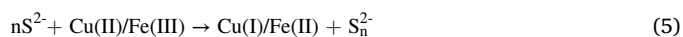
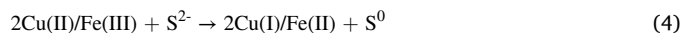


Fig. 5. (a) Total DOS of Fe_3S_4 and $\text{Cu}_{0.5}\text{Fe}_{2.5}\text{S}_4$. (b) Calculated d-band center and p-band center of Fe_3S_4 and $\text{Cu}_{0.5}\text{Fe}_{2.5}\text{S}_4$. (c) Bader charge analysis of Fe_3S_4 and $\text{Cu}_{0.5}\text{Fe}_{2.5}\text{S}_4$ for pristine and $\cdot\text{OH}$ intermediates. (d) Potential schematics. (e) Proposed reaction mechanism for $\text{Cu}_{0.5}\text{Fe}_{2.5}\text{S}_4$ catalyzed H₂O₂ treatment at mild pH.

within Fe_3S_4 is less pronounced, and the Fe atom also experiences some charge loss. This outcome emphasizes the electron shuttle role of Cu atoms in enhancing the internal electron transfer during the HEF process, enabling Fe atoms to retain an electron-rich state (Fig. 5c). This phenomenon is attributed to the sharp and narrow d-band of Cu, which crosses the Fermi energy level and aligns well with the d-band of Fe. Consequently, the strong electronic coupling between them triggers an efficient electron transfer from Cu to Fe [58]. Indeed, the thermodynamic feasibility of Cu(I)-mediated reduction of Fe(III) corroborates this mechanism. The thermodynamically more stable electronic configuration of Cu(II)-S compared to Cu(I)-S also contributes to the electron donor-shuttle regime [59]. The Cu cycle serves as an electron shuttle not only due to its appropriate redox potential, which establishes a robust electron transfer route between S and Fe, but also because the Cu(II) formed can be efficiently reduced by H_2O_2 (Eq. 3) (Fig. 5d). This agrees with our observation that the degradation efficiency of NPX is proportional to the Cu content (in the context of sufficient Fe content) (Fig. S17).

Based on the above results, Fig. 5e highlights the detailed catalytic mechanism of the $\text{Cu}_{0.5}\text{Fe}_{2.5}\text{S}_4$ -catalyzed HEF process for NPX degradation. The in-situ generated H_2O_2 at the cathode is favorably adsorbed and efficiently activated by the active Fe(II) sites in $\text{Cu}_{0.5}\text{Fe}_{2.5}\text{S}_4$ to produce abundant $\cdot\text{OH}$ for the destruction of NPX molecules. The S^{2-} species in $\text{Cu}_{0.5}\text{Fe}_{2.5}\text{S}_4$ acts as the electron donor to ensure the efficient

regeneration of Fe(II) (Eqs. 4–6). More importantly, the Cu species acts as the electron shuttle to accelerate the internal electron transfer between S and Fe, enabling the promotion in Fe(III)/Fe(II) redox cycling (Eqs. 4–7), and the Cu doping can reduce the activation energy of H_2O_2 and initiate the Fenton-like reaction (Eq. 8) to form $\cdot\text{OH}$ [8]. As a result, Eq. 2 is no longer the rate-limiting step of the $\text{Cu}_{0.5}\text{Fe}_{2.5}\text{S}_4$ -catalyzed HEF system because Fe(II) regeneration is greatly boosted. Besides, the unique framework of $\text{Cu}_{0.5}\text{Fe}_{2.5}\text{S}_4$ that inherited from the MIL-88B(Fe) precursor allows the uniform dispersion of the metal active sites and robust structural integrity to ensure the stability of the catalyst during the HEF treatment.



3.4. Practicability of $\text{Cu}_{0.5}\text{Fe}_{2.5}\text{S}_4$

The performance of $\text{Cu}_{0.5}\text{Fe}_{2.5}\text{S}_4$ -catalyzed HEF process was further

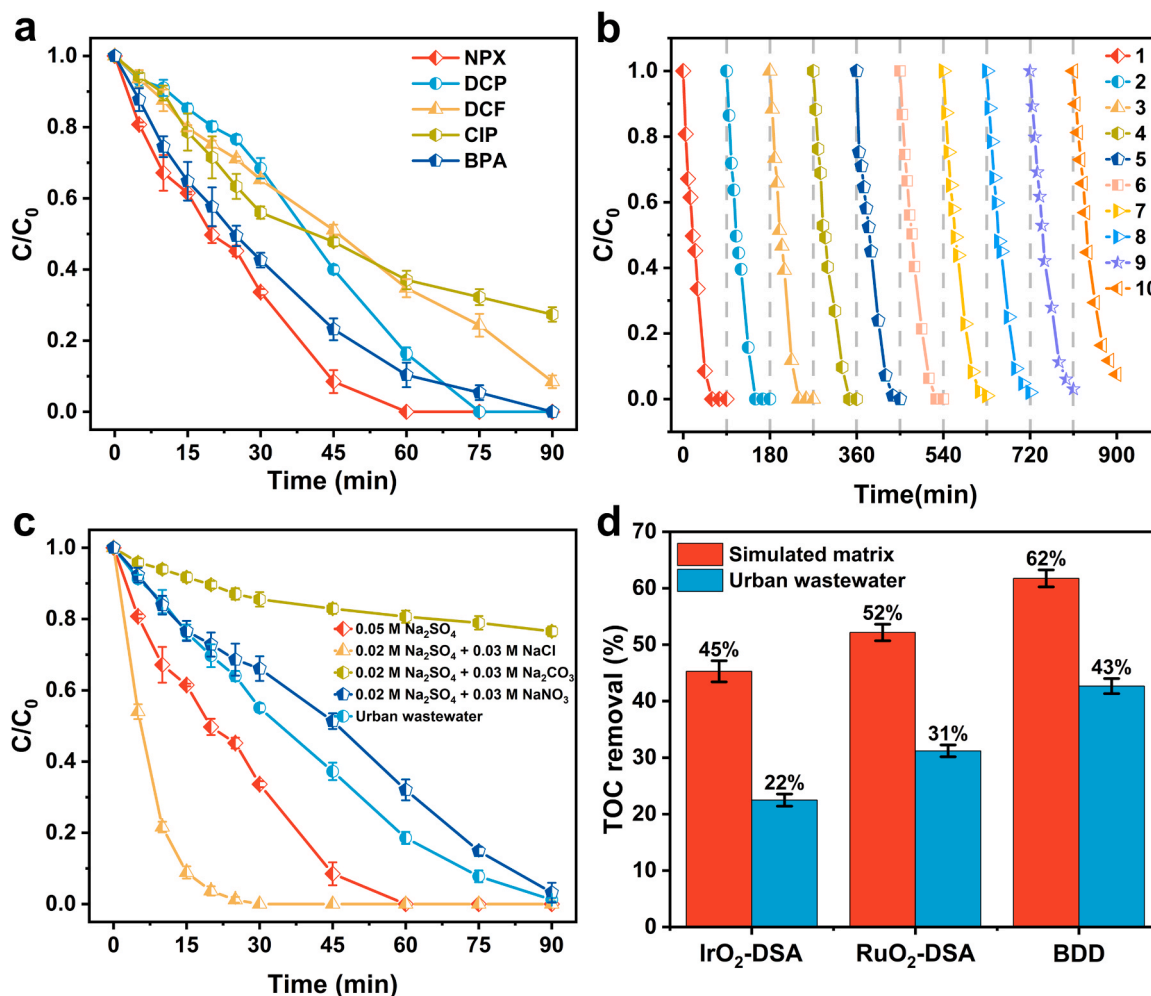


Fig. 6. (a) The degradation performance of $\text{Cu}_{0.5}\text{Fe}_{2.5}\text{S}_4$ catalyzed HEF system considering different target pollutants (160 mL, 10 mg L⁻¹ C pollutants, 0.05 M Na_2SO_4). (b) Degradation of NPX in different batch runs in the $\text{Cu}_{0.5}\text{Fe}_{2.5}\text{S}_4$ catalyzed HEF system. (c) Degradation of NPX during $\text{Cu}_{0.5}\text{Fe}_{2.5}\text{S}_4$ catalyzed HEF in the presence of inorganic anions or in urban wastewater. (d) TOC removal during HEF treatment of NPX using IrO_2 -DSA, RuO_2 -DSA or BDD anode in 0.02 M Na_2SO_4 + 0.03 M NaCl solution or urban wastewater. General conditions: $[\text{NPX}]_0 = 0.060$ mM; $[\text{Catalyst}] = 0.10$ g L⁻¹; Current = 50 mA; initial pH = 7.0.

evaluated by treating different micropollutants at initial pH 7.0. As shown in Fig. 6a, the total removal of NPX, bisphenol A (BPA), 2,4-dichlorophenol (DCP) can be achieved at 90 min, whereas slight lower degradation efficiencies of 91.5% and 72.6% were observed for diclofenac sodium (DCF) and ciprofloxacin (CIP), respectively. The high performances in degrading different pollutants validate the feasibility of $\text{Cu}_{0.5}\text{Fe}_{2.5}\text{S}_4$ -catalyzed HEF process. Nonetheless, the physicochemical properties of the target pollutants like electron affinity can also impact their migration and reactivity with $\cdot\text{OH}$ in water, resulting in different degradation kinetics [60]. In addition, the recyclability of $\text{Cu}_{0.5}\text{Fe}_{2.5}\text{S}_4$ was assessed from ten consecutive trials for NPX degradation. As illustrated in Fig. 6b, the NPX abatement can be attained over 92.5% after ten successive runs, demonstrating the excellent recyclability of the $\text{Cu}_{0.5}\text{Fe}_{2.5}\text{S}_4$ catalyst. Despite the continuous depletion of S^{2-} during the reaction, its strong electron-donating capacity still supported the efficient reduction of metal sites (Eqs. 4–6), allowing the excellent recyclability of the catalyst. The slight decrease in the degradation rate can be attributed to the possible deactivation of the metal active sites [61].

To further elucidate the practicability of $\text{Cu}_{0.5}\text{Fe}_{2.5}\text{S}_4$ catalyzed HEF system, the effects of various inorganic anions that widely coexisted in wastewater, including Cl^- , CO_3^{2-} and NO_3^- , were investigated (Fig. 6c). The presence of 0.03 M NaCl greatly accelerated the NPX destruction, achieving overall abatement in only 30 min, which was ascribed to the partial NPX oxidation by active chlorine formed at the anode surface [62]. In contrast, the addition of 0.03 M Na_2CO_3 led to a very poor NPX abatement, reaching only 23.4% removal at 90 min, because CO_3^{2-} can act as the $\cdot\text{OH}$ scavenger, yielding the $\text{CO}_3^{\cdot-}$ radical with much weaker redox potential [63]. Besides, the presence of 0.03 M NaNO_3 also slowed down the NPX decay because NO_3^- can compete for $\cdot\text{OH}$ to form NO_3^{\cdot} with low redox potential [64]. The applicability of $\text{Cu}_{0.5}\text{Fe}_{2.5}\text{S}_4$ was also evaluated by treating NPX in urban wastewater (Fig. 6c). The complete removal of NPX was achieved in 90 min, slower than that in the Na_2SO_4 matrix due to the competitively consumption of $\cdot\text{OH}$ by natural organic matter in urban wastewater [64].

The TOC abatement during the $\text{Cu}_{0.5}\text{Fe}_{2.5}\text{S}_4$ catalyzed HEF process was assessed as well with different anodes (IrO_2 -DSA, RuO_2 -DSA or BDD) in both simulated matrix and urban wastewater. As shown in Fig. 6d, the presence of natural organic matter in urban wastewater inhibited the TOC decay. The TOC removal efficiencies in both water matrices with different anodes were found to follow the order: IrO_2 -DSA < RuO_2 -DSA < BDD. The RuO_2 -DSA can yield high amounts of active chlorine in the presence of Cl^- to enhance the mineralization, leading to a substantial increase in TOC removal as compared to that with IrO_2 -DSA [62]. The TOC decay was further promoted by replacing the anode with BDD due to the production of strong oxidizing physisorbed BDD ($\cdot\text{OH}$), which can efficiently mineralize the small recalcitrant organics [20]. Consequently, the as-formed active species at the anode and the $\cdot\text{OH}$ produced via the Fenton's reaction together contributed to a satisfactory TOC abatement although the residual TOC still presented in the final solution due to the accumulation of small persistent organics.

4. Conclusions

In this work, a robust $\text{Cu}_{0.5}\text{Fe}_{2.5}\text{S}_4$ catalyst was prepared using MIL88B(Fe) as the precursor to address the rate-limiting step of Fe(II) regeneration in the HEF system. The dual active sites containing catalyst overcomes the drawbacks of the conventional strategies regarding low stability, unsustainability and secondary contamination. As a result, the $\text{Cu}_{0.5}\text{Fe}_{2.5}\text{S}_4$ -catalyzed HEF process demonstrates excellent degradation efficiencies for diverse micropollutants with very low metal leaching and satisfactory reusability. The high performance was due to the S/Cu mediated electron donor-shuttle regime, where S^{2-} species acts as the electron donor to provide sufficient electrons and the Cu species acts as the electron shuttle to facilitate the internal electron transfer between S and Fe, accelerating Fe(III)/Fe(II) circulation. The excellent performances in urban wastewater matrix warrant the great potential of the

$\text{Cu}_{0.5}\text{Fe}_{2.5}\text{S}_4$ /HEF system for practical application.

CRediT authorship contribution statement

Chao Wang: Conceptualization, Data curation, Investigation, Validation; **Wenfeng Zhang:** Data curation, Investigation, Validation; **Jingwen Wang:** Data curation, Investigation; **Pan Xia:** Investigation, Formal analysis; **Xiaoguang Duan:** Methodology, Supervision, Writing – review & editing; **Qiang He:** Resources, Supervision; **Ignasi Sirés:** Supervision, review and editing; **Zhihong Ye:** Conceptualization, Funding acquisition, Investigation, Methodology, Project administration, Resources, Supervision, Writing – original draft.

Declaration of Competing Interest

The authors declare that they have no known competing financial interests or personal relationships that could have appeared to influence the work reported in this paper.

Data availability

Data will be made available on request.

Acknowledgments

This work was supported by the National Natural Science Foundation of China (No. 52100073), the PhD Gateway Program of Chongqing, (CSTB2022BSXM-JCX0140), the Natural Science Foundation of Chongqing, (CSTB2022NSCQ-MSX0432) and the Venture and Innovation Support Program for Chongqing Overseas Returnees (cx2022048, China). I.S. acknowledges financial support from projects PID2019-109291RB-I00, PID2022-140378OB-I00 and PDC2022-133624-I00 (MCIN/AEI/10.13039/501100011033, Spain).

Appendix A. Supporting information

Supplementary data associated with this article can be found in the online version at doi:10.1016/j.apcatb.2023.123457.

References

- [1] S.A. Ismail, W.L. Ang, A.W. Mohammad, Electro-Fenton technology for wastewater treatment: a bibliometric analysis of current research trends, future perspectives and energy consumption analysis, *J. Water Process Eng.* 40 (2021), 101952, <https://doi.org/10.1016/j.jwpe.2021.101952>.
- [2] P.V. Nidheesh, S.O. Ganiyu, C.A. Martínez-Huitle, E. Mousset, H. Olvera-Vargas, C. Trellu, M. Zhou, M.A. Oturan, Recent advances in electro-Fenton process and its emerging applications, *Crit. Rev. Environ. Sci. Technol.* 53 (2022) 887–913, <https://doi.org/10.1080/10643389.2022.2093074>.
- [3] H. Luo, Y. Zeng, D. He, X. Pan, Application of iron-based materials in heterogeneous advanced oxidation processes for wastewater treatment: a review, *Chem. Eng. J.* 407 (2021), 127191, <https://doi.org/10.1016/j.cej.2020.127191>.
- [4] M. Azfar Shaida, S. Verma, S. Talukdar, N. Kumar, M. Salim Mahtab, M. Naushad, I. Haq Farooqi, Critical analysis of the role of various iron-based heterogeneous catalysts for advanced oxidation processes: a state of the art review, *J. Mol. Liq.* 374 (2023), 121259, <https://doi.org/10.1016/j.molliq.2023.121259>.
- [5] Z. Chen, G. Liu, W. Cao, L. Yang, L. Zhang, S. Zhang, J. Zou, R. Song, W. Fan, S. Luo, D.D. Dionysiou, Amorphous low-coordinated cobalt sulphide nanosheet electrode for electrochemically synthesizing hydrogen peroxide in acid media, *Appl. Catal. B Environ.* 334 (2023), 122825, <https://doi.org/10.1016/j.apcatb.2023.122825>.
- [6] M. Liu, Z. Feng, X. Luan, W. Chu, H. Zhao, G. Zhao, Accelerated Fe^{2+} regeneration in an effective electro-Fenton process by boosting internal electron transfer to a nitrogen-conjugated Fe(III) complex, *Environ. Sci. Technol.* 55 (2021) 6042–6051, <https://doi.org/10.1021/acs.est.0c08018>.
- [7] Z. Luo, M. Liu, D. Tang, Y. Xu, H. Ran, J. He, K. Chen, J. Sun, High H_2O_2 selectivity and enhanced Fe^{2+} regeneration toward an effective electro-Fenton process based on a self-doped porous biochar cathode, *Appl. Catal. B Environ.* 315 (2022), 121523, <https://doi.org/10.1016/j.apcatb.2022.121523>.
- [8] C. Ling, X. Liu, H. Li, X. Wang, H. Gu, K. Wei, M. Li, Y. Shi, H. Ben, G. Zhan, C. Liang, W. Shen, Y. Li, J. Zhao, L. Zhang, Atomic-layered Cu_5 nanoclusters on FeS_2 with dual catalytic sites for efficient and selective H_2O_2 activation, *Angew. Chem. Int. Ed.* 61 (2022) 1–8, <https://doi.org/10.1002/anie.202200670>.

- [9] L. Xu, L. Meng, X. Zhang, X. Mei, X. Guo, W. Li, P. Wang, L. Gan, Promoting $\text{Fe}^{3+}/\text{Fe}^{2+}$ cycling under visible light by synergistic interactions between P25 and small amount of Fenton reagents, *J. Hazard. Mater.* 379 (2019), 120795, <https://doi.org/10.1016/j.jhazmat.2019.120795>.
- [10] Y. Xu, P. Xia, C. Wang, J. Cai, H. Li, Z. Ye, H. Zhang, A mini-review on MOFs activated peroxide processes and the enhancement with the external energy, *Chem. Eng. J.* 462 (2023), 142021, <https://doi.org/10.1016/j.cej.2023.142021>.
- [11] H. Zhou, H. Zhang, Y. He, B. Huang, C. Zhou, G. Yao, B. Lai, Critical review of reductant-enhanced peroxide activation processes: trade-off between accelerated $\text{Fe}^{3+}/\text{Fe}^{2+}$ cycle and quenching reactions, *Appl. Catal. B Environ.* 286 (2021), 119900, <https://doi.org/10.1016/j.apcatb.2021.119900>.
- [12] S. Krishnan, C.A. Martínez-Huitle, P.V. Nidheesh, An overview of chelate modified electro-Fenton processes, *J. Environ. Chem. Eng.* 10 (2022), 107183, <https://doi.org/10.1016/j.jece.2022.107183>.
- [13] Z. Ye, E. Brillas, F. Centellas, P.L. Cabot, I. Sirés, Electro-Fenton process at mild pH using Fe(III) -EDDS as soluble catalyst and carbon felt as cathode, *Appl. Catal. B Environ.* 257 (2019), 117907, <https://doi.org/10.1016/j.apcatb.2019.117907>.
- [14] M. Xing, W. Xu, C. Dong, Y. Bai, J. Zeng, Y. Zhou, J. Zhang, Y. Yin, Metal sulfides as excellent Co-catalysts for H_2O_2 decomposition in advanced oxidation processes, *Chem. Commun.* 4 (2018) 1359–1372, <https://doi.org/10.1016/j.chempr.2018.03.002>.
- [15] D. Fan, Y. Lan, P.G. Tratnyek, R.L. Johnson, J. Filip, D.M. O'Carroll, A. Nunez Garcia, A. Agrawal, Sulfidation of iron-based materials: a review of processes and implications for water treatment and remediation, *Environ. Sci. Technol.* 51 (2017) 13070–13085, <https://doi.org/10.1021/acs.est.7b04177>.
- [16] X. Tian, T. Luo, Y. Nie, J. Shi, Y. Tian, D.D. Dionysiou, Y. Wang, New Insight into a Fenton-like reaction mechanism over sulfidated $\beta\text{-FeOOH}$: Key role of sulfidation in efficient iron(III) reduction and sulfate radical generation, *Environ. Sci. Technol.* 56 (2022) 5542–5551, <https://doi.org/10.1021/acs.est.2c00132>.
- [17] H. Wang, T. Chen, D. Chen, X. Zou, M. Li, F. Huang, F. Sun, C. Wang, D. Shu, H. Liu, Sulfurized oolitic hematite as a heterogeneous Fenton-like catalyst for tetracycline antibiotic degradation, *Appl. Catal. B Environ.* 260 (2020), 118203, <https://doi.org/10.1016/j.apcatb.2019.118203>.
- [18] Metal-organic frameworks (MOFs) and their derivatives as emerging catalysts for electro-Fenton process in water purification, in: T. Hu, L. Tang, H. Feng, J. Zhang, X. Li, Y. Zuo, Z. Lu, W. Tang (Eds.), *Coord. Chem. Rev.* 451, 2022, 214277, <https://doi.org/10.1016/j.ccr.2021.214277>.
- [19] Metal-organic frameworks for highly efficient heterogeneous Fenton-like catalysis, in: M. Cheng, C. Lai, Y. Liu, G. Zeng, D. Huang, C. Zhang, L. Qin, L. Hu, C. Zhou, W. Xiong (Eds.), *Coord. Chem. Rev.* 368, 2018, pp. 80–92, <https://doi.org/10.1016/j.ccr.2018.04.012>.
- [20] Z. Ye, W. Zhang, S. Lanzalaco, L. Zhao, I. Sirés, P. Xia, J. Zhai, Q. He, Ultra-uniform MIL-88B(Fe)/ Fe_3S_4 hybrids engineered by partial sulfidation to boost catalysis in electro-Fenton treatment of micropollutants: Experimental and mechanistic insights, *Chem. Eng. J.* 455 (2023), <https://doi.org/10.1016/j.cej.2022.140757>.
- [21] G.A. Kifle, Y. Huang, M. Xiang, W. Wang, C. Wang, C. Li, H. Li, Heterogeneous activation of peroxymonosulfate by iron-based bimetallic nanostructures for the efficient remediation of contaminated water. A review, *Chem. Eng. J.* 442 (2022), 136187, <https://doi.org/10.1016/j.cej.2022.136187>.
- [22] Y. Li, B. Yao, Y. Chen, Y. Zhou, X. Duan, Metal-organic frameworks (MOFs) as efficient catalysts for electro-Fenton (EF) reactions: current progress and prospects, *Chem. Eng. J.* 463 (2023), 142287, <https://doi.org/10.1016/j.cej.2023.142287>.
- [23] Y. Xiang, H. Liu, E. Zhu, K. Yang, D. Yuan, T. Jiao, Q. Zhang, S. Tang, Application of inorganic materials as heterogeneous cocatalyst in Fenton/Fenton-like processes for wastewater treatment, *Sep. Purif. Technol.* 295 (2022), 121293, <https://doi.org/10.1016/j.seppur.2022.121293>.
- [24] Z. Wang, Y. Du, P. Zhou, Z. Xiong, C. He, Y. Liu, H. Zhang, G. Yao, B. Lai, Strategies based on electron donors to accelerate $\text{Fe(III)}/\text{Fe(II)}$ cycle in Fenton or Fenton-like processes, *Chem. Eng. J.* 454 (2023), <https://doi.org/10.1016/j.cej.2022.140096>.
- [25] J. Li, A.N. Pham, R. Dai, Z. Wang, T.D. Waite, Recent advances in Cu-Fenton systems for the treatment of industrial wastewaters: role of Cu complexes and Cu composites, *J. Hazard. Mater.* 392 (2020), 122261, <https://doi.org/10.1016/j.jhazmat.2020.122261>.
- [26] J. Tang, J. Wang, MOF-derived three-dimensional flower-like $\text{FeCu}@C$ composite as an efficient Fenton-like catalyst for sulfamethazine degradation, *Chem. Eng. J.* 375 (2019), 122007, <https://doi.org/10.1016/j.cej.2019.122007>.
- [27] Y. Wang, H. Zhao, G. Zhao, Iron-copper bimetallic nanoparticles embedded within ordered mesoporous carbon as effective and stable heterogeneous Fenton catalyst for the degradation of organic contaminants, *Appl. Catal. B Environ.* 164 (2015) 396–406, <https://doi.org/10.1016/j.apcatb.2014.09.047>.
- [28] P. Cao, K. Zhao, X. Quan, S. Chen, H. Yu, Efficient and stable heterogeneous electro-Fenton system using iron oxides embedded in Cu, N co-doped hollow porous carbon as functional electrocatalyst, *Sep. Purif. Technol.* 238 (2020), 116424, <https://doi.org/10.1016/j.seppur.2019.116424>.
- [29] J. Zhang, H. Zeng, L. Bu, S. Zhou, S. Shi, L. Deng, CuO incorporated cobalt/nitrogen doped carbonaceous frameworks derived from ZIF-67 ($\text{Cu}@C\text{-N-C}$) as PMS activator for efficient degradation of naproxen: Direct electron transfer and $^1\text{O}_2$ dominated nonradical mechanisms, *Chem. Eng. J.* 454 (2023), 139989, <https://doi.org/10.1016/j.cej.2022.139989>.
- [30] P. Xia, Z. Ye, L. Zhao, Q. Xue, S. Lanzalaco, Q. He, X. Qi, I. Sirés, Tailoring single-atom FeN_4 moieties as a robust heterogeneous catalyst for high-performance electro-Fenton treatment of organic pollutants, *Appl. Catal. B Environ.* 322 (2023), <https://doi.org/10.1016/j.apcatb.2022.122116>.
- [31] M.A. Oturan, Outstanding performances of the BDD film anode in electro-Fenton process: applications and comparative performance, *Curr. Opin. Solid State Mater. Sci.* 25 (2021), 100925, <https://doi.org/10.1016/j.cossms.2021.100925>.
- [32] Y.H. Li, C.C. Wang, F. Wang, W. Liu, L. Chen, C. Zhao, H. Fu, P. Wang, X. Duan, Nearly zero peroxydisulfate consumption for persistent aqueous organic pollutants degradation via nonradical processes supported by in-situ sulfate radical regeneration in defective MIL-88B(Fe), *Appl. Catal. B Environ.* 331 (2023), 122699, <https://doi.org/10.1016/j.apcatb.2023.122699>.
- [33] Z. Yang, Z. Wang, J. Wang, Y. Li, G. Zhang, Facet-dependent activation of oxalic acid over magnetic recyclable Fe_3S_4 for efficient pollutant removal under visible light irradiation: enhanced catalytic activity, DFT calculations, and mechanism insight, *Environ. Sci. Technol.* 56 (2022) 18008–18017, <https://doi.org/10.1021/acs.est.2c06571>.
- [34] W. Shi, J. Ma, F. Gao, R. Dai, X. Su, Z. Wang, Metal-organic framework with a redox-active bridge enables electrochemically highly selective removal of arsenic from water, *Environ. Sci. Technol.* (2022), <https://doi.org/10.1021/acs.est.2c09683>.
- [35] J. Hang, X.H. Yi, C.C. Wang, H. Fu, P. Wang, Y. Zhao, Heterogeneous photo-Fenton degradation toward sulfonamide matrix over magnetic Fe_3S_4 derived from MIL-100 (Fe), *J. Hazard. Mater.* 424 (2022), 127415, <https://doi.org/10.1016/j.jhazmat.2021.127415>.
- [36] N.M. Mahmoodi, J. Abdi, M. Taghizadeh, A. Taghizadeh, B. Hayati, A.A. Shekarchi, M. Vossoughi, Activated carbon/metal-organic framework nanocomposite: Preparation and photocatalytic dye degradation mathematical modeling from wastewater by least squares support vector machine, *J. Environ. Manag.* 233 (2019) 660–672, <https://doi.org/10.1016/j.jenvman.2018.12.026>.
- [37] J. Li, Q. Liu, G. Gou, S. Kang, X. Tan, B. Tan, L. Li, N. Li, C. Liu, B. Lai, New insight into the mechanism of peroxymonosulfate activation by Fe_3S_4 : Radical and non-radical oxidation, *Sep. Purif. Technol.* 286 (2022), 120471, <https://doi.org/10.1016/j.seppur.2022.120471>.
- [38] A. Gu, K. Chen, X. Zhou, C. Gong, P. Wang, Y. Jiao, P. Mao, K. Chen, J. Lu, Y. Yang, Trimetallic MOFs-derived Fe-Co-Cu oxycarbide toward peroxymonosulfate activation for efficient trichlorophenol degradation via high-valent metal-oxo species, *Chem. Eng. J.* 468 (2023), 143444, <https://doi.org/10.1016/j.cej.2023.143444>.
- [39] X. Lin, K. Shih, J. Chen, X. Xie, Y. Zhang, Y. Chen, Z. Chen, Y. Li, Insight into flower-like greigite-based peroxydisulfate activation for effective bisphenol A abatement: performance and electron transfer mechanism, *Chem. Eng. J.* 391 (2020), 123558, <https://doi.org/10.1016/j.cej.2019.123558>.
- [40] W. Liu, L. Jin, J. Xu, J. Liu, Y. Li, P. Zhou, C. Wang, R.A. Dahlgren, X. Wang, Insight into pH dependent Cr(VI) removal with magnetic Fe_3S_4 , *Chem. Eng. J.* 359 (2019) 564–571, <https://doi.org/10.1016/j.cej.2018.11.192>.
- [41] N.K. Shrestha, S.A. Patil, A.S. Salunke, A.I. Inamdar, H. Im, Accelerating glucose electrolysis on Cu-doped MIL-88B for an energy efficient anodic reaction in water splitting, *Dalt. Trans.* 52 (2023) 10933–10941, <https://doi.org/10.1039/d3dt01773g>.
- [42] H. Wang, B. Liao, M. Hu, Y. Ai, L. Wen, S. Yang, Z. Ye, J. Qin, G. Liu, Heterogeneous activation of peroxymonosulfate by natural chalcopyrite for efficient remediation of groundwater polluted by aged landfill leachate, *Appl. Catal. B Environ.* 300 (2022), 120744, <https://doi.org/10.1016/j.apcatb.2021.120744>.
- [43] S. Shi, X. Han, J. Liu, X. Lan, J. Feng, Y. Li, W. Zhang, J. Wang, Photothermal-boosted effect of binary Cu-Fe bimetallic magnetic MOF heterojunction for high-performance photo-Fenton degradation of organic pollutants, *Sci. Total Environ.* 795 (2021), 148883, <https://doi.org/10.1016/j.scitotenv.2021.148883>.
- [44] J. Li, X. Zhang, M. Liu, B. Pan, W. Zhang, Z. Shi, X. Guan, Enhanced reactivity and electron selectivity of sulfidated zerovalent iron toward chromate under aerobic conditions, *Environ. Sci. Technol.* 52 (2018) 2988–2997, <https://doi.org/10.1021/acs.est.7b06502>.
- [45] E.E. Oguzie, J. Li, Y. Liu, D. Chen, Y. Li, K. Yang, F. Wang, The effect of Cu addition on the electrochemical corrosion and passivation behavior of stainless steels, *Electrochim. Acta* 55 (2010) 5028–5035, <https://doi.org/10.1016/j.electacta.2010.04.015>.
- [46] Z. Feng, J. Yang, L. Zhu, T. Sun, Bromine functionalized Fe/Cu bimetallic MOFs for accelerating $\text{Fe(III)}/\text{Fe(II)}$ cycle and efficient degradation of phenol in Fenton-like system, *Colloids Surf. A Physicochem. Eng. Asp.* 658 (2023), 130701, <https://doi.org/10.1016/j.colsurfa.2022.130701>.
- [47] M. Villanueva-Rodríguez, A. Hernández-Ramírez, J.M. Peralta-Hernández, E. R. Bandala, M.A. Quiroz-Alfaro, Enhancing the electrochemical oxidation of acid-yellow 36 azo dye using boron-doped diamond electrodes by addition of ferrous ion, *J. Hazard. Mater.* 167 (2009) 1226–1230, <https://doi.org/10.1016/j.jhazmat.2008.12.137>.
- [48] Z. Ye, R. Oriol, C. Yang, I. Sirés, X.Y. Li, A novel $\text{NH}_2\text{-MIL-88B(Fe)}$ -modified ceramic membrane for the integration of electro-Fenton and filtration processes: A case study on naproxen degradation, *Chem. Eng. J.* 433 (2022), <https://doi.org/10.1016/j.cej.2021.133547>.
- [49] J. Li, T. Yang, G. Zeng, L. An, J. Jiang, Z. Ao, J. Ma, Ozone- and hydroxyl radical-induced degradation of micropollutants in a novel UVA-LED-activated periodate advanced oxidation process, *Environ. Sci. Technol.* (2022), <https://doi.org/10.1021/acs.est.2c06414>.
- [50] Y. Yang, Y. Xia, F. Wei, G. Teng, Y. Yao, Preparation and characterization of hydrophobic stearic acid-Yb-PbO₂ anode and its application on the electrochemical degradation of naproxen sodium, *J. Electroanal. Chem.* 868 (2020), 114191, <https://doi.org/10.1016/j.jelechem.2020.114191>.
- [51] W. Tan, W. Ren, C. Wang, Y. Fan, B. Deng, H. Lin, H. Zhang, Peroxymonosulfate activated with waste battery-based Mn-Fe oxides for pollutant removal: Electron transfer mechanism, selective oxidation and LFER analysis, *Chem. Eng. J.* 394 (2020), 124864, <https://doi.org/10.1016/j.cej.2020.124864>.

- [52] S.C. Mei, L. Li, G.X. Huang, X.Q. Pan, H.Q. Yu, Heterogeneous Fenton water purification catalyzed by iron phosphide (FeP), *Water Res.* 241 (2023), 120151, <https://doi.org/10.1016/j.watres.2023.120151>.
- [53] X. Du, W. Fu, P. Su, J. Cai, M. Zhou, Internal-micro-electrolysis-enhanced heterogeneous electro-Fenton process catalyzed by Fe/Fe₃C@PC core-shell hybrid for sulfamethazine degradation, *Chem. Eng. J.* 398 (2020), 125681, <https://doi.org/10.1016/j.cej.2020.125681>.
- [54] K. Yang, Z. Zhai, H. Liu, T. Zhao, D. Yuan, T. Jiao, Q. Zhang, S. Tang, Peracetic acid activation by natural chalcopryrite for metronidazole degradation: unveiling the effects of Cu-Fe bimetallic sites and sulfur species, *Sep. Purif. Technol.* 305 (2023), 122500, <https://doi.org/10.1016/j.seppur.2022.122500>.
- [55] X. Gao, J. Feng, D. Su, Y. Ma, G. Wang, H. Ma, J. Zhang, In-situ exfoliation of porous carbon nitride nanosheets for enhanced hydrogen evolution, *Nano Energy* 59 (2019) 598–609, <https://doi.org/10.1016/j.nanoen.2019.03.016>.
- [56] S. Lu, X. Li, Y. Cheng, J. Zhou, G. Zhang, In situ electrogenerated Cu(III) triggers hydroxyl radical production on the Cu-Sb-SnO₂ electrode for highly efficient water decontamination, *Proc. Natl. Acad. Sci.* 120 (2023), e2306835120, <https://doi.org/10.1073/pnas.2306835120>.
- [57] W. Qu, Z. Tang, S. Tang, H. Wen, J. Fang, Q. Lian, D. Shu, C. He, Cation substitution induced d-Band center modulation on cobalt-based spinel oxides for catalytic ozonation, *Adv. Funct. Mater.* (2023), <https://doi.org/10.1002/adfm.202301677>.
- [58] M. Song, J. Han, Y. Wang, L. Chen, Y.Y. Chen, X. Liao, Effects and mechanisms of Cu species in Fe-MOFs on Fenton-like catalytic activity and stability, *ACS Appl. Mater. Interfaces* 15 (2023) 36201–36213, <https://doi.org/10.1021/acsami.3c05928>.
- [59] J. Huang, Y. Zhou, S. Deng, Y. Shangguan, R. Wang, Q. Ge, X. Feng, Z. Yang, Y. Ji, T. Fan, B. Chen, B. Li, C. Zheng, X. Hu, H. Chen, Photo-assisted reductive cleavage and catalytic hydrolysis-mediated persulfate activation by mixed redox-couple-involved CuFeS₂ for efficient trichloroethylene oxidation in groundwater, *Water Res.* 222 (2022), 118885, <https://doi.org/10.1016/j.watres.2022.118885>.
- [60] J.L. Wang, L.J. Xu, Advanced oxidation processes for wastewater treatment: formation of hydroxyl radical and application, *Crit. Rev. Environ. Sci. Technol.* 42 (2012) 251–325, <https://doi.org/10.1080/10643389.2010.507698>.
- [61] J. Yang, R. Huang, Y. Cao, H. Wang, A. Ivanets, C. Wang, Heterogeneous Fenton degradation of persistent organic pollutants using natural chalcopryrite: effect of water matrix and catalytic mechanism, *Environ. Sci. Pollut. Res.* 29 (2022) 75651–75663, <https://doi.org/10.1007/s11356-022-21105-0>.
- [62] G. Coria, I. Sirés, E. Brillas, J.L. Nava, Influence of the anode material on the degradation of naproxen by Fenton-based electrochemical processes, *Chem. Eng. J.* 304 (2016) 817–825, <https://doi.org/10.1016/j.cej.2016.07.012>.
- [63] L. Zhao, Y. Chen, Y. Feng, D. Wu, Oxidation of acetaminophen by Green rust coupled with Cu(II) via dioxygen activation: the role of various interlayer anions (CO₃²⁻, SO₄²⁻, Cl⁻), *Chem. Eng. J.* 350 (2018) 930–938, <https://doi.org/10.1016/j.cej.2018.06.039>.
- [64] X. Du, W. Fu, P. Su, Q. Zhang, M. Zhou, S-doped MIL-53 as efficient heterogeneous electro-Fenton catalyst for degradation of sulfamethazine at circumneutral pH, *J. Hazard. Mater.* 424 (2022), 127674, <https://doi.org/10.1016/j.jhazmat.2021.127674>.